

Magnetic Resonance Imaging of T_2 - and Diffusion Anisotropy Using a Tilttable Receive Coil



Chantal M. W. Tax, Elena Kleban, Muhamed Baraković,
Maxime Chamberland, and Derek K. Jones

Abstract The anisotropic microstructure of white matter is reflected in various MRI contrasts. Transverse relaxation rates can be probed as a function of fibre-orientation with respect to the main magnetic field, while diffusion properties are probed as a function of fibre-orientation with respect to an encoding gradient. While the latter is easy to obtain by varying the orientation of the gradient, as the magnetic field is fixed, obtaining the former requires re-orienting the head. In this work we deployed a tilttable RF-coil to study T_2 - and diffusional anisotropy of the brain white matter simultaneously in diffusion- T_2 correlation experiments.

C. M. W. Tan and E. Kleban share first authorship.

C. M. W. Tax (✉) · E. Kleban · M. Chamberland · D. K. Jones
Cardiff University Brain Research Imaging Centre (CUBRIC), Cardiff University, Cardiff, UK
e-mail: TaxC@cardiff.ac.uk

E. Kleban
e-mail: KlebanE@cardiff.ac.uk

M. Chamberland
e-mail: ChamberlandM@cardiff.ac.uk

D. K. Jones
e-mail: JonesD27@cardiff.ac.uk

M. Baraković
Cardiff University Brain Research Imaging Centre (CUBRIC), Cardiff University, Cardiff, UK
e-mail: muhamed.barakovic@epfl.ch

Signal Processing Laboratory 5, Ecole Polytechnique Federale de Lausanne, Lausanne, Switzerland

Translational Imaging in Neurology Basel, Department of Biomedical Engineering, University Hospital Basel, Basel, Switzerland

© The Author(s) 2021

E. Özarslan et al. (eds.), *Anisotropy Across Fields and Scales*,

Mathematics and Visualization, https://doi.org/10.1007/978-3-030-56215-1_12

1 Introduction

1.1 Background

Magnetic Resonance Imaging (MRI) allows us to probe structural anisotropy of tissue *in vivo* by studying the magnetic properties and translational motion of for instance hydrogen protons. In the human body, hydrogen is naturally abundant in various compounds, with the highest MR signal amplitude detected from hydrogen in water molecules. Hydrogen protons possess spin angular momentum, which is an intrinsic quantum property that allows the occurrence of magnetic interactions and resonance. When placed in a magnetic field, there is a slight preference for spins to be aligned with the field, resulting in a net magnetisation \mathbf{M} aligned with the main magnetic field \mathbf{B}_0 [1]. Upon the application of a radiofrequency field at the Larmor frequency \mathbf{B}_1 , \mathbf{M} can be tipped out of alignment with \mathbf{B}_0 ; most commonly into the perpendicular plane. The measured signal is the result of the ensemble of spins precessing coherently in the plane, and signal loss (decay) occurs when such coherence reduces.

This signal decay, which results from a progressive loss of coherence of precessional phase, i.e. *dephasing*, is also called spin-spin relaxation. The spin-spin relaxation rate is usually denoted by $R_2 = 1/T_2$, where T_2 is the time taken for the magnetization to decay to $1/e$ of its initial value [2, 3]. In addition to the irreversible spin-spin relaxation, dephasing can be caused by local variations in the magnetic field, a reversible process if the spins are static. Such local variations in the magnetic field arise from a difference in interaction of different substances with the magnetic field (*susceptibility effects*). If the spins experience Brownian molecular motion, they will experience various magnetic field strengths, and their dephasing due to local field changes will be effectively irreversible. Hence, the measured apparent T_2 of signal decay will no longer be purely induced by dephasing due to spin-spin interactions, but will depend on the amplitude and spatial characteristics of the local field variations, and the mean displacement of molecules per unit of time due to incoherent motion.

In diffusion-weighted MRI, additional (and typically much stronger) magnetic field variations are induced intentionally by applying *magnetic field gradients* which cause the strength of the main magnetic field \mathbf{B}_0 to vary linearly in space [4–6]. As such, the Brownian molecular motion can be encoded in the signal in a controlled way.

The interplay of susceptibility and diffusion effects leads to the anisotropy of tissue being reflected in different MRI contrasts and hence the combination of contrasts can give a more complete picture of tissue microstructure. In the following paragraphs we will describe anisotropy in the brain and these processes in more detail.

Structural anisotropy of human brain tissue. The dominant tissue exhibiting anisotropy in the brain is the *white matter* (WM). It is predominantly composed of the long extensions of neuronal cells—the axons, which are grouped into

fibre bundles and inter-connect different areas of the brain. The main function of axons is to transmit electric impulses between and within brain areas. Axons can be insulated by a *myelin sheath* which is formed of lipid chains and allows a faster signal transmission. The size, density, length of the axons and their myelination levels vary with age and may alter with pathology. Therefore, investigation of the white matter microstructure is of high importance in understanding the functionality of the healthy brain, but also in studying the mechanisms of normal/abnormal development and pathology.

Diffusion effects. Measurements of Brownian molecular motion in biological tissue can reflect not only the temperature and the viscosity of the medium it is occurring in, but most importantly will be sensitive to the underlying geometry and anisotropy of the tissue. For instance, in the brain white matter water molecules can propagate much easier along fibre bundles than perpendicular to them because of obstacles such as the cell membrane and myelin [7]. This property can be used to estimate the main orientation of fibre bundles and their virtual reconstruction by means of *fibre tractography* [8, 9]. Additionally, if water molecules are trapped inside the axon and cannot penetrate the boundaries (restricted diffusion), the mean displacement perpendicular to the axon will be similar to its diameter at long diffusion times. The diffusion of water molecules which reside outside axons is commonly thought of as not being fully restricted but hindered. An example of the differences between the movement of water molecules residing inside and outside of axons is visualised in Fig. 1a.

In MRI, Brownian motion of water molecules is most commonly encoded using a pair of pulsed magnetic field gradients, a dephasing and a rephasing gradient [6] (Fig. 2). If spins are stationary, these gradients would have no additional effect on the signal decay. However if spins change their positions during or between the application of the gradients, the rephasing will be incomplete which will result in signal loss. The signal loss due to diffusion can be enhanced by increasing the magnitude of the gradients, the time during which the gradients are on, and/or the time between the gradients. The strength of the diffusion weighting is described by the *b*-value; a parameter which combines the information on the diffusion gradient strength and timings.

Magnetic susceptibility effects. Any material placed inside a strong magnetic field interacts with it—it can become magnetised itself. The proportionality constant linking magnetic field strength and the magnetisation induced inside the material is called *magnetic susceptibility*. At the boundaries between materials with different magnetic properties the magnetic flux density is spatially inhomogeneous and its distribution will depend on the boundary orientation to the magnetic field and the difference in susceptibility between the materials. Additionally, the magnetisation induced in some materials may also depend on the orientation of the sample to the magnetic field, i.e. the magnetic susceptibility of those materials is anisotropic.

As mentioned above, the nerve fibres in human brain are insulated by myelin sheath. Myelin is more diamagnetic than water, i.e., it is repelled more strongly by a magnetic field. Additionally, several studies suggested that the magnetic suscepti-

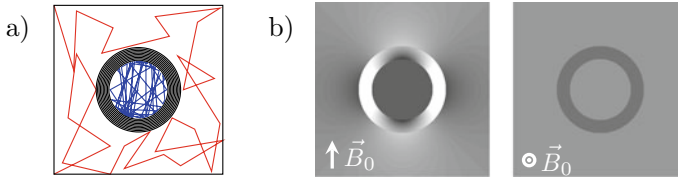


Fig. 1 A white matter nerve fibre can be modelled as a hollow cylinder composed of a myelin sheath. **a** Brownian motion perpendicular to the nerve fibre is restricted inside the cylinder (the molecules are “trapped” inside the cylinder) and hindered outside of it (the mean displacement of the molecules per time-point is larger, but nevertheless lower than ‘free’ water). **b** The myelin sheath is more diamagnetic than the surrounding tissue and perturbs the local magnetic field. The field perturbation is inhomogeneous and depends on the nerve fibre orientation to the magnetic field \mathbf{B}_0

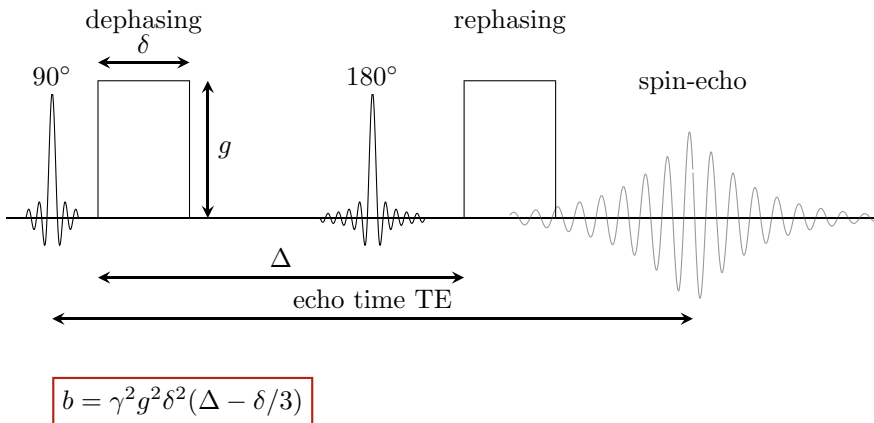


Fig. 2 Pulsed-gradient spin-echo sequence: the echo time TE is defined as the time between the radio-frequency pulse and the centre of the spin-echo. The diffusion-weighting strength, the b -value, can be calculated as $b = \gamma^2 g^2 \delta^2 (\Delta - \delta/3)$

bility of the myelin sheath has an anisotropic component [10–12]. It has been shown that the signal decay from white matter varies as a function of orientation to \mathbf{B}_0 [13–20] and can be well explained using a hollow cylinder fibre model (Fig. 1b) [17] and is often represented by a 3-pool model [18, 21, 22].

The strongest contribution to this signal anisotropy arises from the water trapped between the layers of myelin sheath, called the myelin water. However, the myelin water signal decays very quickly, on account of its short T_2 (~ 10 – 30 ms), and is usually negligible at the echo times used in a typical diffusion-weighted MRI experiment. Nevertheless, it has also been observed that signal decay rates may still be orientation-dependent even without this myelin-water component [13, 20, 23–25].

1.2 Scope of This Work

In myelinated white matter it has been reported that T_2^* (where $1/T_2^* = 1/T_2 + 1/T_2'$ and T_2' can be understood as capturing the reversible effects of field inhomogeneities) depends on the orientation of the fibre with respect to \mathbf{B}_0 due to microscopic susceptibility effects [13, 16, 18, 19, 26]. Orientation-dependence of T_2 was also reported recently [20, 23, 24, 27] and could potentially characterise microscopic-susceptibility more reliably and reflect effects related to axon diameter [24, 28]. Experiments designed to probe relaxation-anisotropy commonly involve reorienting the head inside the scanner, and are thus challenged by unintended signal-to-noise ratio (SNR) variations across orientations caused by differences in proximities to the receiver coil, and by increased susceptibility to motion and artefacts due to patient-discomfort. In this work, we re-purpose a tiltable RF coil (originally designed for patient comfort) to investigate T_2 -orientational dependence within the context of a diffusion- T_2 correlation experiment. The coil can be tilted around the left-right axis by 0° , 9° and 18° to \mathbf{B}_0 , which: (1) minimises patient-discomfort and thus improves reliability; (2) offers a new degree of freedom as tilting around the left-right axis is otherwise difficult to achieve; (3) fixes the coil-to-brain distance across orientations and thus reduces SNR variations; and (4) increases the reproducibility of the experiment.

Finally, instead of studying global variations across the whole brain volume, we adopt an along-tract profiling *tractometry* approach (i.e., which is the mapping of measures along pathways reconstructed with tractography [29, 30]) to assess spatial variations in more detail.

2 Methods

2.1 Data Acquisition

The study was approved by the Cardiff University School of Psychology Ethics Committee and written informed consent was obtained. Two healthy volunteers (female, 30 y.) were scanned on a 3 T 300 mT/m Connectom scanner equipped with a modified 20-channel head/neck tiltable coil (Siemens Healthcare, Erlangen, Germany). Each subject was in supine, head first position and the direction of the magnetic field \mathbf{B}_0 was along the superior-inferior radiological axis. MRI data were acquired in the default (0°) and tilted (18°) orientations of the tiltable coil (Fig. 3a, b). One of the subjects underwent a second scan in the default head orientation to examine test-retest variability.

Diffusion- T_2 correlation data were acquired using a pulsed-gradient spin-echo echo-planar-imaging (PGSE-EPI) sequence [6] (Fig. 2), with different echo-times TE to probe T_2 , and diffusion-weighting strengths or b -values to probe diffusion, (Fig. 3c). The timings of the diffusion encoding gradients were fixed for all echo

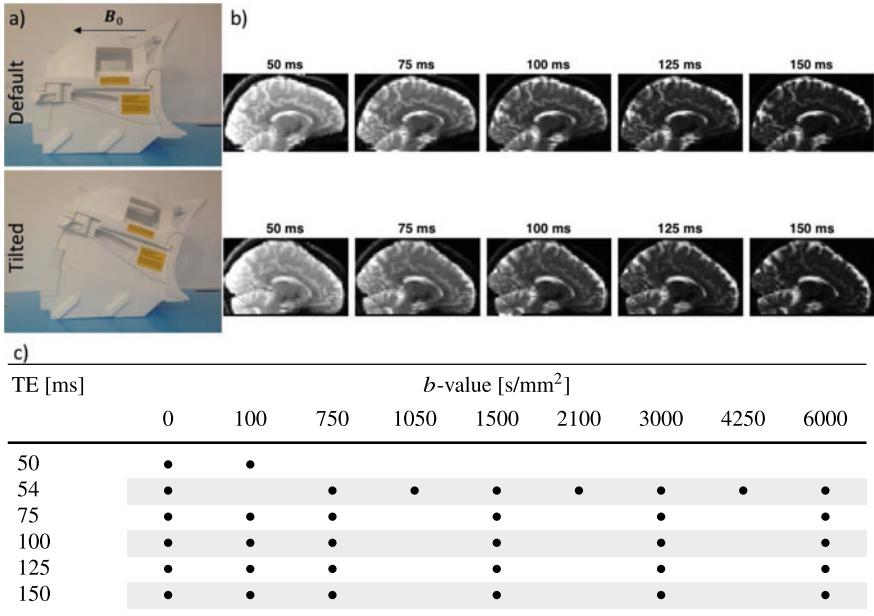


Fig. 3 a The coil in default (0°) and tilted (18°) position. b $b = 0\text{ s/mm}^2$ images at different TE. c Acquisition parameters for the diffusion-correlation experiment

times. The signal in voxel \mathbf{x} can then be denoted as $S_{\mathbf{x}}(b, TE)$. Additional b_0 -images were acquired in the halfway-tilted (9°) position (not shown). Remaining parameters were repetition time TR 3.5 s and voxel size $3 \times 3 \times 3\text{ mm}^3$.

2.2 MRI Signal Processing

The diffusion- T_2 data were preprocessed to correct for subject motion, eddy current effects, Gibbs ringing and gradient non-linearities [31–33] for each subject and each head orientation. Spatial correspondence between the tilted and default head orientations was obtained in two ways: 1) by nonlinear registration [34] to the halfway-tilted (9°) space, and 2) by a tractometry approach in native space.

The tractometry [29] approach in native space of each head orientation relied on the quantitative mapping of measures along reconstructed brain pathways. First, fibre orientation distribution functions (fODFs) [35, 36] were estimated at each voxel using multi-tissue multi-shell constrained spherical deconvolution (MSMT-CSD) [37]. For each coil position, peaks were extracted from the resulting fODFs and used as input to perform streamline tractography on the $TE = 54\text{ ms}$ data. Bundles were automatically segmented [38], a representative core-streamline was computed [39], and the bundles were subsequently subdivided [40, 41] into $n = 20$ segments (s)

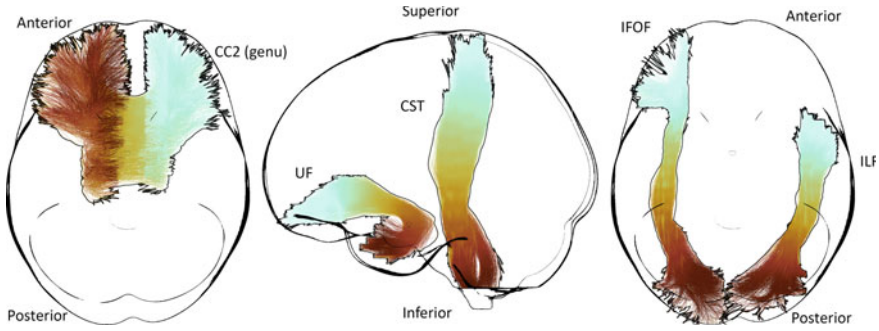


Fig. 4 Extracted brain pathways of interest from subject 2. Bundles were segmented into 20 sections (0: light-blue, 20: dark-brown). CC: corpus callosum, UF: uncinate fasciculus, CST: corticospinal tract, IFOF: inferior fronto-occipital fasciculus, ILF: inferior longitudinal fasciculus. Visualisation was performed using FiberNavigator [43]

(Fig. 4). Voxels with a single-fibre-population were identified [42] and assigned to s_i if their location was inside the segment and their orientation was within 30° of the orientation of the core-streamline in that segment. Note that only tract-segments with minimal fanning (assessed visually) were considered. T_2 values were then profiled for each bundle independently by taking the mean and standard error of the mean within each tract segment.

2.3 Estimation

SNR estimates were obtained from the background of the images acquired at $TE = 54$ ms and $b = 0$ s/mm² for both the (0°) and (18°) coil-orientations [44]. The voxel-wise T_2 was estimated from the b_0 -signals as $S(0, TE) = S(0, 0)e^{-TE/T_2}$, using a nonlinear least-squares trust-region-reflective algorithm in Matlab.

Fibre orientation θ to the main magnetic field \mathbf{B}_0 was estimated for the voxels with single fibre population. With prior knowledge of θ orientation-dependent (anisotropic) and -independent (isotropic) components of R_2 can be estimated as follows [20, 45]: $R_2(\theta) = R_{2,\text{isotropic}} + R_{2,\text{anisotropic}} \cdot \sin^4 \theta$.

3 Results

Signal-to-noise ratio. The estimated noise standard deviation was similar for the two coil-orientations. Figure 5a compares the signals in the default and the tilted position after registration to the common space; the signal (and thus SNR) between coil-orientations varied within a similar range as the range seen between test-retest scans in

the same orientation. Globally, the images are aligned but some local misalignments can still be observed.

Voxel-wise T_2 -estimates. Figure 5b highlights differences in estimated T_2 for different coil-orientations. Globally, the difference in T_2 -values estimated from the data in default and tilted head orientations is larger than or equal to T_2 -values estimated from test-retest scans in default head orientation for subject 1 (Fig. 5b, left half). Local differences in T_2 can be observed between the default and tilted position, as indicated by red arrows in the T_2 -maps in Fig. 5b, for example. The inverse T_2 -values in white matter mostly range between 9 s^{-1} and 21 s^{-1} for both subjects and head orientation.

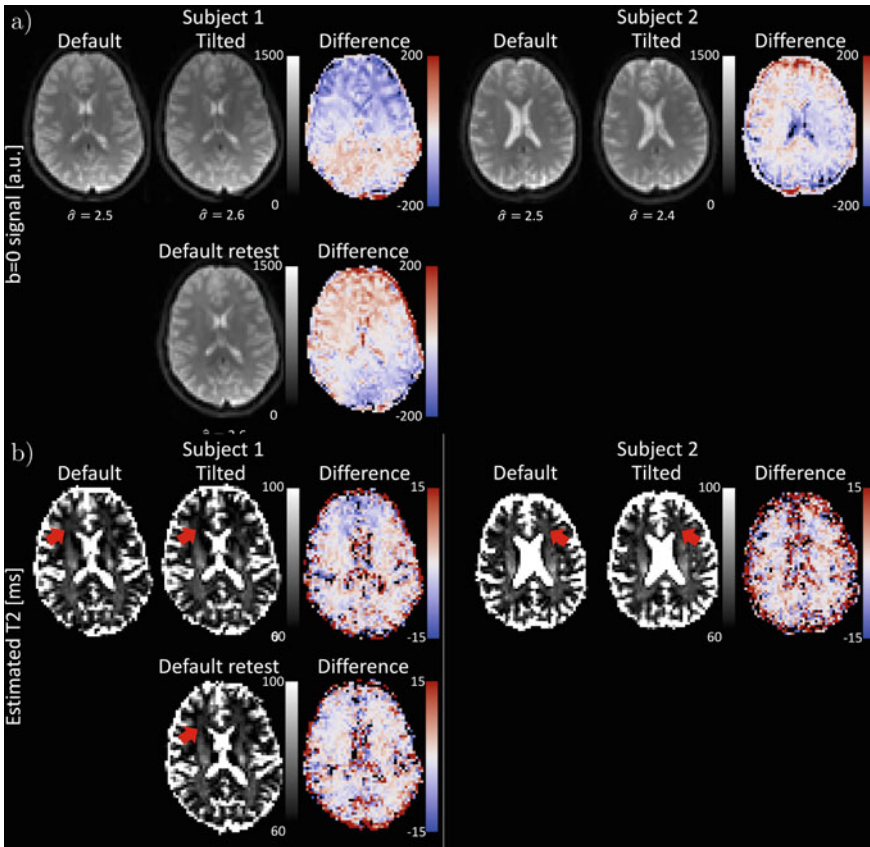


Fig. 5 **a** $b = 0\text{ s/mm}^2$ image for the default (0°) and tilted (18°) orientation registered to the half-way-tilted (9°) space, and their difference (tilted—default). $\hat{\sigma}$ is the estimated standard deviation in the background of the image. **b** Estimated T_2 for the default (0°) and tilted (18°) orientation registered to the half-way-tilted (9°) space, and their difference. Red arrows indicate regions of visible difference

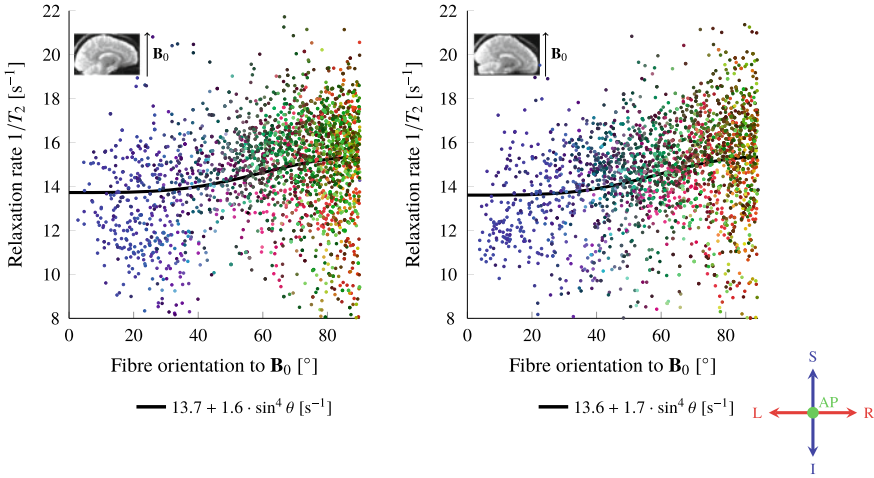


Fig. 6 Relaxation rate $1/T_2$ as a function of the fibre-orientation θ with the main magnetic field, in the default (left) and tilted (right) position. Each point represents a single-fibre-population voxel and is colour-coded according to its orientation (red, blue, and green correspond to the left-right, superior-inferior and anterior-posterior axis, respectively). The black line represents a model-fit of $1/T_2$ as a function of θ as described in previous literature and references therein [13, 19, 20]

Global WM isotropic and anisotropic T_2 -stimates. The total isotropic (orientation-independent) component of relaxation rate of $R_2 = 1/T_2$ in WM was estimated at $13.7 \pm 0.2 \text{ s}^{-1}$ and $13.6 \pm 0.2 \text{ s}^{-1}$, in default and tilted head orientations, respectively, for one of the subjects (Fig. 6). For the same subject the total WM anisotropic components of the inverse T_2 were $1.6 \pm 0.25 \text{ s}^{-1}$ and $1.7 \pm 0.25 \text{ s}^{-1}$, for default and tilted head positions, respectively. The range of T_2 -values in white matter and their total isotropic and anisotropic components are consistent with previously reported values in [20, 45].

Tractometry analysis. Figures 7, 8 and 9 show the along-tract profiles of the estimated T_2 (top plot) and angle w.r.t. \mathbf{B}_0 (bottom plot) for different tracts. Globally, the angular profiles show comparable characteristics between subjects in the default and tilted position. For Subject 1, the angular profiles remain similar in the default and default-retest acquisition, except for the inferior parts of the corticospinal tract (CST).

Profiling of T_2 in the CST, which runs along the z -axis (i.e., inferosuperior), reveals a significant increase in T_2 , for example in segment 16 which experiences a change in orientation w.r.t. \mathbf{B}_0 from $\sim 35^\circ$ in the default position to $\sim 55^\circ$ in the tilted position (Fig. 7). This is in the regime where the derivative of the relaxation rate $1/T_2$ as a function of angle is the largest (Fig. 6). The uncinate fasciculus (UF) shows a noisier pattern, likely because the number of single-fibre voxels per segment is generally lower ($\sim 5-10$ in the UF compared to $\sim 15-20$ in the CST).

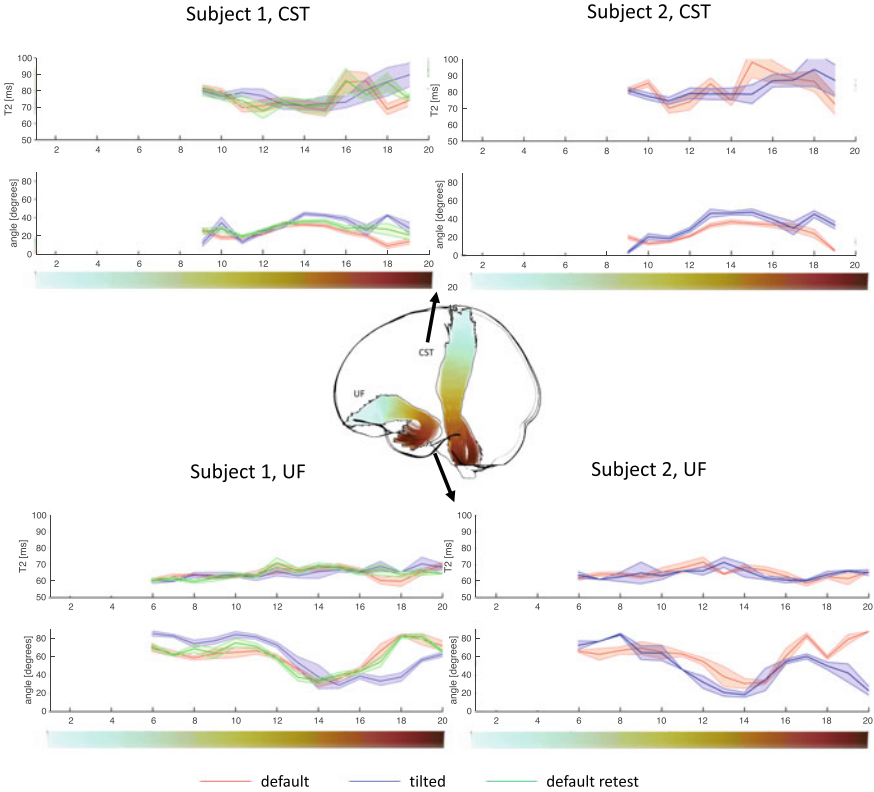


Fig. 7 Tractometry results (mean and standard error) for the corticospinal tract (CST, top plots) and the uncinate fasciculus (UF, bottom plots). T_2 -values and fibre orientation to \mathbf{B}_0 are plotted against segment numbers for each fibre tract and subject. Colour bar indicates tract-segment location, corresponding to the colour-encoding on the visualised tracts. Note that only tract-segments with minimal fanning (assessed visually) were considered

In the inferior longitudinal fasciculus (ILF) (Fig. 8) a global decrease in angle w.r.t. \mathbf{B}_0 from default to tilted position leads to an overall, yet subtle, increase in T_2 . In the inferior fronto-occipital fasciculus (IFOF) the pattern is less clear.

In the callosal midbody the angle w.r.t. \mathbf{B}_0 remains relatively unchanged and so does T_2 .

4 Discussion

In this work we have incorporated a tiltable coil in T_2 -diffusion-correlation experiment to modulate the white matter fibre orientation with respect to the main magnetic field \mathbf{B}_0 .

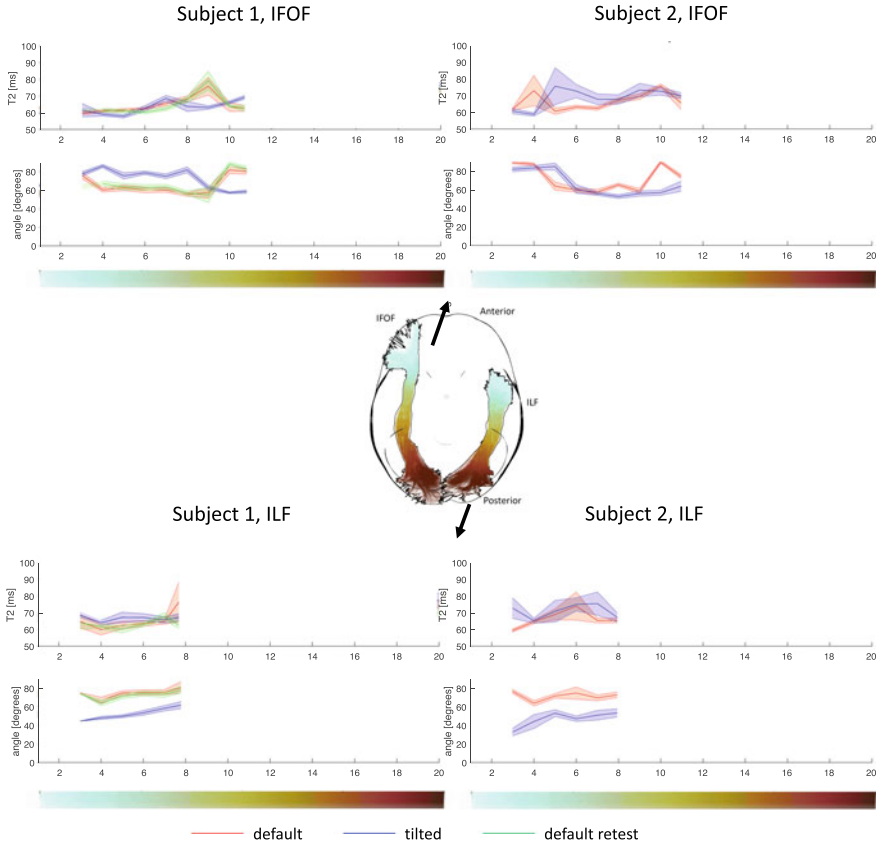


Fig. 8 Tractometry results (mean and standard error) for the inferior fronto-occipital fasciculus (IFOF, top plots) and the inferior longitudinal fasciculus (ILF, bottom plots). T_2 -values and fibre orientation to \mathbf{B}_0 are plotted against segment numbers for each fibre tract and subject. Colour bar indicates tract-segment location, corresponding to the colour-encoding on the visualised tracts. Note that only tract-segments with minimal fanning (assessed visually) were considered

We observed changes in the T_2 -tract-profile after the participants' heads were re-oriented in the scanner, with up to ~ 10 ms difference in T_2 -values between the default and the tilted head orientation. The test-retest T_2 -tract profiles in the default head position are more similar to each-other than to the tract profiles in the tilted head position, as for example evident from the results for the CST and IFOF. These initial results suggest variation of T_2 as a function of fibre orientation to \mathbf{B}_0 and that tilting the participant's head by 18° can reveal those variations.

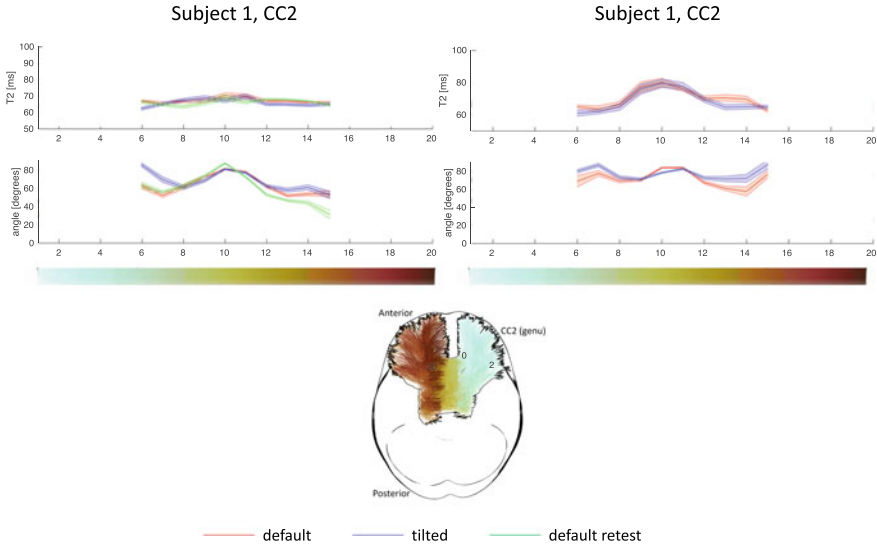


Fig. 9 Tractometry results for the genu of the corpus callosum (CC2). T_2 -values and fibre orientation to \mathbf{B}_0 are plotted against segment numbers for each subject. Colour bar corresponds to tract-segment location, and this is colour-encoded on the tracts themselves. Note that only tract-segments with minimal fanning (assessed visually) were considered

4.1 Incorporating Tiltable Coil in T_2 -diffusion correlation experiments

Robustness of experimental setup when using a tiltable coil. The tiltable coil allows us to control the pitch orientation of the participant’s head. We have demonstrated an overall test-retest similarity of estimated fibre-tract orientations in the default position, whereas there were clear differences with the tilted head position. However, some differences in fibre orientation of the CST between the test and retest could be observed, particularly in the inferior segments, while differences in fibre orientation in the IFOF tract were less obvious. Given the apparent stability of the IFOF tract profiling and insensitivity of fibre orientation to the head rotation around \mathbf{B}_0 in the default head position (yaw), the test-retest differences in the CST could be a result of an additional roll head orientation with respect to the coil between the two scans. Such additional differences in orientation could be mitigated by further restricting head position within the coil, e.g. additional padding or performing the experiments with differences in tilt immediately after each other without a break. Whereas this introduces a confound in assessing test-retest variability, the estimation of fibre-orientations is done in each coil orientation independently and as such we do not expect this to be detrimental in the overall assessment of T_2 -anisotropy.

Range of orientations. By re-purposing a coil that was designed to maximise patient comfort in clinical situations means that the range of coil orientations was limited. A

larger range of orientations would allow the θ versus $1/T_2$ relationship to be elucidated more robustly. Nevertheless, these initial experiments demonstrate the utility of this hardware design for uncovering orientational-anisotropy effects in vivo.

4.2 *Origin of T_2 -Contrast and -Anisotropy in WM*

The water signal from each WM voxel is a superposition of the signal from different water pools (e.g. intra- and extra-axonal, and at short TE also myelin water), therefore the macroscopic T_2 -values measured in this study could be approximated as the weighted average of the T_2 -values from each of the two compartments. This means that the macroscopic T_2 will depend on individual T_2 -values of the compartments, but also on the relative contribution to the signal. As such, tracts with the same apparent T_2 but differences in signal fractions and T_2 -values between the intra- and the extra-axonal compartments could exhibit very different apparent orientational anisotropy.

A clear separation of macroscopic T_2 -values in some tracts and segments between the default and the tilted head orientations suggests that macroscopic T_2 is also a function of orientation to \mathbf{B}_0 . Fibre tract re-orientation in the magnetic field will cause local changes in the local magnetic field due to differences between the magnetic susceptibility of the myelin sheath and the surrounding tissue. Following the hollow-cylinder model [26], the magnitude of these microscopic \mathbf{B}_0 -field perturbations is expected to be larger in the extra-axonal compartment and, in combination with molecular Brownian motion, will cause an additional faster relaxation in the extra-axonal compartment [46]. Future work will explore the effects of fibre orientation on individual compartments [47, 48].

4.3 *Considerations in Data Processing*

Tractometry versus image registration In this work we adopted tract profiling for comparing the T_2 -diffusion-correlation data in default and tilted head positions, instead of a voxel-based analysis; image registration was used for visualisation purposes only. Voxel-based analysis is known to suffer from confounds related to mis-registration and data interpolation, an effect we visually observed in our study likely amplified by the large imaging voxels (3 mm isotropic) and imperfect correction for geometric distortions due to gradient nonlinearities. With the tractometry approach, spatial correspondence between coil orientations was established while keeping the data in native space, and each segment constitutes information from multiple voxels improving robustness to noise. We were able to reproduce T_2 -values from test-retest along the tracts.

Correction for subject motion The individual images have been corrected for subject motion, which could also involve head re-orientation with respect to the magnetic field. Subjects who participated in this study were experienced MR scanner participants, therefore the maximum rotation around any axis rarely exceeded 1.5° . However, when considering the application of this method on less compliant subjects, subject motion could become a confounding factor.

5 Conclusion

Including a tiltable coil into the experimental set-up for diffusion- T_2 correlation measurements paves the way for a more reliable assessment of orientational T_2 dependence. Microstructural origins of the differences in T_2 could include differences in pathway properties (e.g. axon diameter) or susceptibility effects. T_2 orientational-dependence would furthermore impact analyses frameworks that assume constant T_2 along pathways [49]. Voxel-wise comparison of T_2 from different head-orientations remains challenging due to complications in experiment setup, imperfect correction for geometric distortions, and intrinsic scan-variability. Using a tractometry framework, we found indications of regional changes in T_2 upon tilting of the head. Studying this effect in a larger population is necessary to increase statistical power. In future work, the diffusion- T_2 correlation experiments can be used to study compartmental T_2 orientation-dependence.

Acknowledgments CMWT is supported by a Rubicon grant (680-50-1527) from the Netherlands Organisation for Scientific Research (NWO) and a Sir Henry Wellcome Fellowship (215944/Z/19/Z). DKJ, CMWT and MC were all supported by a Wellcome Trust Investigator Award (096646/Z/11/Z) and DKJ was supported by a Wellcome Strategic Award (104943/Z/14/Z).

The data were acquired at the UK National Facility for In Vivo MR Imaging of Human Tissue Microstructure funded by the EPSRC (grant EP/M029778/1), and The Wolfson Foundation.

We are grateful to Fabrizio Fasano, Peter Gall, and Matschl Volker from Siemens Healthcare GmbH for their support.

References

1. Hanson, L.G.: Concepts Magn. Reson. Part A **32A**(5), 329 (2008). <https://doi.org/10.1002/cmra.20123>
2. Bloch, F.: Phys. Rev. (1946). <https://doi.org/10.1103/PhysRev.70.460>
3. Hahn, E.L.: Phys. Rev. **80**(4), 580 (1950). <https://doi.org/10.1103/PhysRev.80.580>
4. Carr, H.Y., Purcell, E.M.: Phys. Rev. (1954). <https://doi.org/10.1103/PhysRev.94.630>
5. Torrey, H.C.: Phys. Rev. (1956). <https://doi.org/10.1103/PhysRev.104.563>
6. Stejskal, E.O., Tanner, J.E.: J. Chem. Phys. **42**(1), 288 (1965). <https://doi.org/10.1063/1.1695690>
7. Beaulieu, C.: NMR Biomed. Int. J. Devoted Develop. Appl. Magn. Reson. Vivo **15**(7–8), 435 (2002)

8. Conturo, T.E., Lori, N.F., Cull, T.S., Akbudak, E., Snyder, A.Z., Shimony, J.S., McKinstry, R.C., Burton, H., Raichle, M.E.: *Proc. Natl. Acad. Sci.* **96**(18), 10422 (1999)
9. Jeurissen, B., Descoteaux, M., Mori, S., Leemans, A.: *NMR Biomed.* **32**(4), e3785 (2019)
10. Liu, C.: *Magn. Reson. Med.* **63**(6), 1471 (2010). <https://doi.org/10.1002/mrm.22482>, <https://doi.org/10.1002/mrm.22482doi.wiley.com/10.1002/mrm.22482>
11. Lee, J., Shmueli, K., Fukunaga, M., van Gelderen, P., Merkle, H., Silva, A.C., Duyn, J.H.: *Proc. Natl. Acad. Sci.* **107**(11), 5130 (2010). <https://doi.org/10.1073/pnas.0910222107>
12. van Gelderen, P., Mandelkow, H., de Zwart, J.A., Duyn, J.H.: *Magn. Reson. Med.* **74**(5), 1388 (2015). <https://doi.org/10.1002/mrm.25524>, <https://onlinelibrary.wiley.com/doi/abs/10.1002/mrm.25524>
13. Bender, B., Klose, U.: *NMR Biomed.* **23**(9), 1071 (2010). <https://doi.org/10.1002/nbm.1534>
14. Denk, C., Torres, E.H., MacKay, A., Rauscher, A.: *NMR Biomed.* **24**(3), 246 (2011). <https://doi.org/10.1002/nbm.1581>
15. Lee, J., van Gelderen, P., Kuo, L.W., Merkle, H., Silva, A.C., Duyn, J.H.: *NeuroImage* **57**(1), 225 (2011). <https://doi.org/10.1016/j.neuroimage.2011.04.026>
16. Van Gelderen, P., De Zwart, J.A., Lee, J., Sati, P., Reich, D.S., Duyn, J.H.: *Magn. Reson. Med.* **67**(1), 110 (2012). <https://doi.org/10.1002/mrm.22990>
17. Wharton, S., Bowtell, R.: *NeuroImage* **83**, 1011 (2013). <https://doi.org/10.1016/j.neuroimage.2013.07.054>
18. Sati, P., van Gelderen, P., Silva, A.C., Reich, D.S., Merkle, H., De Zwart, J.A., Duyn, J.H.: *NeuroImage* **77**, 268 (2013). <https://doi.org/10.1016/j.neuroimage.2013.03.005>
19. Rudko, D.A., Klassen, L.M., De Chickera, S.N., Gati, J.S., Dekaban, G.A., Menon, R.S.: *Proc. Natl. Acad. Sci. U. S. Am.* **111**, 1 (2014). <https://doi.org/10.1073/pnas.1306516111>
20. Gil, R., Khabipova, D., Zwiwers, M., Hilbert, T., Kober, T., Marques, J.P.: *NMR Biomed.* **29**(12), 1780 (2016). <https://doi.org/10.1002/nbm.3616>
21. Thapaliya, K., Vegh, V., Bollmann, S., Barth, M.: *NeuroImage* **182**, 407 (2018). <https://doi.org/10.1016/j.neuroimage.2017.11.029>, <http://www.sciencedirect.com/science/article/pii/S1053811917309436>
22. Tendler, B.C., Bowtell, R.: *Magn. Reson. Med.* **81**(5), 3017 (2019). <https://doi.org/10.1002/mrm.27626>
23. Knight, M.J., Wood, B., Couthard, E., Kauppinen, R.: *Biomed. Spectro. Imaging* **4**(3), 299 (2015). <https://doi.org/10.3233/BSI-150114>, <http://www.medra.org/servelet/aliasResolver?alias=iiospress&doi=10.3233/BSI-150114>
24. McKinnon, E.T., Jensen, J.H.: *Magn. Reson. Med.* **81**(5), 2985 (2019). <https://doi.org/10.1002/mrm.27617>, <http://doi.wiley.com/10.1002/mrm.27617>
25. Kleban, E., Tax, C.M., Rudrapatna, U.S., Jones, D.K., Bowtell, R.: *NeuroImage* **116793**, (2020). <https://doi.org/10.1016/j.neuroimage.2020.116793>, <http://www.sciencedirect.com/science/article/pii/S1053811920302809>
26. Wharton, S., Bowtell, R.: *Proc. Natl. Acad. Sci. U. S. A.* **109**(45), 18559 (2012). <https://doi.org/10.1073/pnas.1211075109>
27. Birkel, C., Doucette, J., Fan, M., Hernandez-Torres, E., Rauscher, A.: *bioRxiv* (2020). <https://doi.org/10.1101/2020.03.11.987925>, <https://www.biorxiv.org/content/early/2020/03/12/2020.03.11.987925>
28. Kaden, E., Alexander, D.C.: *Proceedings of the International Conference on Information Processing in Medical Imaging*, vol. 23, p. 607 (2013). https://doi.org/10.1007/978-3-642-38868-2_51
29. Bells, S., Cercignani, M., Deoni, S., Assaf, Y., Pasternak, O., Evans, C., Leemans, A., Jones, D.K.: *Proceedings of the International Society for Magnetic Resonance in Medicine*, p. 678 (2011)
30. Jones, D.K., Travis, A.R., Eden, G., Pierpaoli, C., Basser, P.J.: *Magn. Reson. Med. Official J. Int. Soc. Magn. Reson. Med.* **53**(6), 1462 (2005)
31. Andersson, J.L.: *Diffusion MRI*, pp. 63–85. Elsevier Inc., (2014). <https://doi.org/10.1016/B978-0-12-396460-1.00004-4>

32. Kellner, E., Dhital, B., Kiselev, V.G., Reiser, M.: *Magn. Reson. Med.* **76**(5), 1574 (2016). <https://doi.org/10.1002/mrm.26054>
33. Rudrapatna, S.U., Parker, G.D., Roberts, J., Jones, D.K.: *ISMRM*, p. 1206 (2018)
34. Avants, B.B., Tustison, N.J., Stauffer, M., Song, G., Wu, B., Gee, J.C.: *Front. Neuroinform.* **8**(APR) (2014). <https://doi.org/10.3389/fninf.2014.00044>
35. Tournier, J.D., Calamante, F., Connelly, A.: *NeuroImage* **35**(4), 1459 (2007). <https://doi.org/10.1016/j.neuroimage.2007.02.016>, <https://linkinghub.elsevier.com/retrieve/pii/S1053811907001243>
36. Descoteaux, M., Deriche, R., Knosche, T.R., Anwander, A.: *IEEE Trans. Med. Imaging* **28**(2), 269 (2008)
37. Jeurissen, B., Tournier, J.D., Dhollander, T., Connelly, A., Sijbers, J.: *NeuroImage* **103**, 411 (2014). <https://doi.org/10.1016/j.neuroimage.2014.07.061>
38. Wasserthal, J., Neher, P., Maier-Hein, K.H.: *NeuroImage* **183**, 239 (2018). <https://doi.org/10.1016/j.neuroimage.2018.07.070>
39. Chamberland, M., St-Jean, S., Tax, C.M., Jones, D.K.: *International Conference on Medical Image Computing and Computer-Assisted Intervention*, pp. 359–366. Springer, Berlin (2018)
40. Cousineau, M., Jodoin, P.M., Morency, F.C., Rozanski, V., Grand'Maison, M., Bedell, B.J., Descoteaux, M.: *NeuroImage: Clin.* **16**, 222 (2017). <https://doi.org/10.1016/j.nicl.2017.07.020>
41. Chamberland, M., Raven, E.P., Genc, S., Duffy, K., Descoteaux, M., Parker, G.D., Tax, C.M., Jones, D.K.: *NeuroImage* **200**, 89 (2019)
42. Tax, C., Jeurissen, B., Vos, S., Viergever, M., Leemans, A.: *NeuroImage* **86**, (2014). <https://doi.org/10.1016/j.neuroimage.2013.07.067>
43. Chamberland, M., Whittingstall, K., Fortin, D., Mathieu, D., Descoteaux, M.: *Front. Neuroinform.* **8**, 59 (2014)
44. Koay, C.G., Özarslan, E., Pierpaoli, C.: *J. Magn. Reson.* **199**(1), 94 (2009). <https://doi.org/10.1016/J.JMR.2009.03.005>, <https://www.sciencedirect.com/science/article/pii/S1090780709000767?via%3Dihub>
45. Knight, M.J., Dillon, S., Jarutyte, L., Kauppinen, R.A.: *Biophys. J.* **112**(7), 1517 (2017). <https://doi.org/10.1016/j.bpj.2017.02.026>
46. Cowan, B.: *Contemp. Phys.* **56**, 1 (2015). <https://doi.org/10.1080/00107514.2015.1005683>
47. Tax, C., Rudrapatna, U., Witzel, T., Jones, D.: *ISMRM*, p. 0838 (2017)
48. Veraart, J., Novikov, D.S., Fieremans, E.: *NeuroImage* **182**, 360 (2018). <https://doi.org/10.1016/J.NEUROIMAGE.2017.09.030>, <https://www.sciencedirect.com/science/article/pii/S1053811917307784?via%3Dihub>
49. Daducci, A., Canales-Rodríguez, E.J., Zhang, H., Dyrby, T.B., Alexander, D.C., Thiran, J.P.: *NeuroImage* **105**, 32 (2015). <https://doi.org/10.1016/J.NEUROIMAGE.2014.10.026>, <https://www.sciencedirect.com/science/article/pii/S1053811914008519?via%3Dihub>

Open Access This chapter is licensed under the terms of the Creative Commons Attribution 4.0 International License (<http://creativecommons.org/licenses/by/4.0/>), which permits use, sharing, adaptation, distribution and reproduction in any medium or format, as long as you give appropriate credit to the original author(s) and the source, provide a link to the Creative Commons licence and indicate if changes were made.

The images or other third party material in this chapter are included in the chapter's Creative Commons licence, unless indicated otherwise in a credit line to the material. If material is not included in the chapter's Creative Commons licence and your intended use is not permitted by statutory regulation or exceeds the permitted use, you will need to obtain permission directly from the copyright holder.

